High-resolution entry and exit surface dosimetry in a 1.5 T MR-linac

Elizabeth Patterson (✉ ep958@uowmail.edu.au)
    University of Wollongong   https://orcid.org/0000-0002-6240-2887

Peter Stokes
    Townsville Hospital

Dean Cutajar
    University of Wollongong

Anatoly Rosenfeld
    University of Wollongong

John Baines
    Townsville Hospital

Peter Metcalfe
    University of Wollongong

Marcus Powers
    Townsville Hospital

Abstract

The magnetic field of a transverse MR-linac alters electron trajectories as the photon beam transits through materials, causing lower doses at flat entry surfaces and increased doses at flat beam-exiting surfaces. This study investigated the response of a MOSFET detector, known as the MO*Skin*™, for high-resolution surface and near-surface percentage depth dose measurements on an Elekta Unity. Simulations with Geant4 and the Monaco treatment planning system (TPS), and EBT-3 film measurements, were also performed for comparison. Measured MO*Skin*™ entry surface doses, relative to d_{max}, were (9.9 ± 0.2) %, (10.1 ± 0.3) %, (11.3 ± 0.6) %, (12.9 ± 1.0) %, and (13.4 ± 1.0) % for 1 × 1 cm^2, 3 × 3 cm^2, 5 × 5 cm^2, 10 × 10 cm^2, and 22 × 22 cm^2 fields, respectively. Similarly at the beam exit MO*Skin*™ doses were (37.2 ± 4.9) %, (50.0 ± 2.9) %, (54.9 ± 2.0) %, (63.9 ± 1.6) %, and (62.4 ± 3.0) %. For the investigated fields, the maximum absolute dose differences for Geant4, TPS, and film at the beam entry, relative to MO*Skin*™ surface doses, were 1.0%, 16.4%, and 24.3%, respectively and at the beam exit, 5.0%, 3.1%, and 5.7%, respectively. The largest increase in exit dose, due to the electron return effect, was 18.0% for the 22 × 22 cm^2 field size, using Geant4 calculations. The results presented in the study validate the suitability of the MO*Skin*™ detector for transverse MR-linac surface dosimetry.

Introduction

Megavoltage (MV) photon beams are typically used to treat deep-seated tumours because of the skin-sparing effect. In recent years image-guided radiation therapy (IGRT) on MV photon treatment systems has developed, and online magnetic resonance-guided radiation therapy (MRgRT), offering superior soft tissue contrast imaging, is now available. Such treatments are delivered by machines known as magnetic resonance (MR)-linacs that provide a non-ionizing form of imaging. One of the two commercially available MR-linac systems is the Elekta Unity (Elekta, Stockholm, Sweden) which integrates a 1.5 T magnetic resonance imaging unit and a linac with a flattening-filter-free (FFF) 7 MV photon beam. For these MR-linacs the radiation beam is perpendicular to the magnetic field direction.

The impact of the transverse magnetic field on secondary electron transport is well established in literature [1]–[3]. Dose perturbations include a lateral shift in the dose distribution and asymmetric penumbra [1], [4], [5], a reduction in the depth of maximum dose (d_{max}) [1], [2], [4]–[7], and the electron return effect (ERE) [2], [4], [8]. There is also evidence that skin-sparing can be enhanced, compared to conventional linac (0 T) treatments, due to the magnetic field sweeping contaminant secondary electrons away from the treatment area [5]–[13]. However, in some situations, such as when the entry and exit surfaces are oblique, this is not the case [8], [9], [11], and the corresponding dose due to the ERE is non-trivial [9], [11].

Previous investigations of near-surface dose in a transverse MR-linac have used dosimeters with varying effective point of measurement (EPOM). These include radiochromic film [6], [14], [15], PTW 31021 Semiflex 3D [16], optically stimulated luminescence dosimeters (OSLDs) [17]–[19], thermoluminescent dosimeters (TLDs) [20], metal-oxide-semiconductor field-effect transistor (MOSFET) [21], gel [22], PTW

60019 microDiamond [6], [14], [16], and a PTW 34045 Advanced Markus chamber [6], [12]. Parallel-plate chambers, such as the Advanced Markus chamber, are commonly used for dose measurements in the build-up region on conventional linacs. For MR-linac dosimetry, the magnetic field influences charge collection in the air-filled sensitive volume (SV) of the ionization chamber [23]. For reference dosimetry, near constant correction factors, specific to the magnetic field, can be applied to ionisation chamber measurements beyond d_{max}; however, in the build-up region correction factors become depth-dependent [24] due to a loss of charged-particle equilibrium (CPE) conditions. With a variable magnetic field correction factor in the build-up region and a SV thickness in the order of millimetres [25], the ionisation chamber is not an ideal dosimeter to accurately measure skin dose in a transverse MR-linac.

The human skin depth recommended for practical dose estimates is 0.07 mm, and corresponds to the average depth of the basal layer that is responsible for producing new skin cells [26]. To accurately measure skin dose, a dosimeter with a small SV and reproducible water equivalent depth (WED) of 0.07 mm should be considered, to avoid volume averaging that can occur in heterogeneous dose regions. Similarly for small-field dosimetry, the size of the SV should be considerably smaller than the field size as a loss of CPE impacts the detectors readings [27]. With skin dose specified at 0.07 mm, previous near-surface dose investigations are lacking as dosimeters with larger EPOMs were used [6], [14]–[19], [21], [22], [28]. The dose averaged across the SV of an OSLD corresponds to a near-skin water equivalent depth (WED) of 0.16 mm, with the external casing of the OSLD removed [17]. Similarly, film positioned at the surface has a WED of 0.14 mm (i.e. half the thickness of a sheet of EBT-3 film).

Of interest is a study that investigated surface and near-surface dose measurements, at the beam entry and exit, in a 1.5 T transverse MR-linac using nanoDot OSLDs (Landauer, Glenwood, USA) [17]. The study reported surface doses, relative to d_{max}, of 15.7%, 16.7%, and 18.0%, at the beam entry, and 56.0%, 62.8%, and 63.4% at the beam exit, for 5×5 cm^2, 10×10 cm^2, and 22×22 cm^2 fields, respectively [17]. The authors commented that further experimental investigations were required since previous film data reported entry surface doses of 34.6% and 35.8%, relative to d_{max}, for field sizes 5×5 cm^2 and 10×10 cm^2, respectively [16].

For accurate Monte Carlo simulations of skin dose, high-resolution scoring is recommended [8]. Unlike experimental dosimeters with a fixed SV, Monte Carlo simulations can be scored according to the user's specifications. Dose calculations at the beam entry and exit for a 6 MV linear accelerator with a 1.5 T transverse magnetic field, have previously been investigated [8]. Using 0.01 mm thick voxels, Monte Carlo calculations determined a sharp increase in dose from 10.0–40.0%, normalised to the dose at d_{max}, in the first millimetre of the build-up region for a 10×10 cm² field. At the beam exit for the same field size, the dose increased from 40.0–55.0%, relative to d_{max}, as a direct consequence of the ERE [8]. Using high-resolution scoring geometry at the beam entry and exit reveals the extent of the dose gradient that otherwise would be masked using a larger dose voxel size. Likewise, using a dosimeter with a large SV, relative to the steep gradient, would cause volume averaging and inaccurate dosimetry.

We propose using a MOSFET detector, called the MO*Skin*™, for surface dosimetry in a 1.5 T transverse MR-linac. MOSFET detectors often have an epoxy bubble to protect the SV; however, the MO*Skin*™ utilises a thin and reproducible polyimide build-up. With a 4.8×10^{-6} mm^3 SV, thickness of 3.0×10^{-4} mm, reproducible water equivalent build-up equal to 0.07 mm, and overall thickness of 0.4 mm (which includes a thin silicon substrate positioned at the rear of the detector [29]), the MO*Skin*™ is an ideal candidate for skin and surface dosimetry. Another benefit of MOSFET technology is the real-time readout of measurements, while dosimeters such as film and OSLD require more stringent preparation and read-out protocols. Additionally, the MO*Skin*™ reportedly experiences no significant readout changes in the presence of a 1.0 T static magnetic field [30]. Previous MR-linac measurements with the MO*Skin*™ on a 1.0 T inline MR-linac show comparable results to Geant4 simulations, film, and a microDiamond detector, demonstrating the suitability of the detector in an MR environment [31]–[33]. Readers wishing for greater detail on the mechanisms behind general MOSFET and MO*Skin*™ dosimetry readout are referred elsewhere [34].

The objective of this study is to use the MO*Skin*™ to experimentally characterise surface and near-surface dose on a 1.5 T transverse MR-linac. The term 'skin dose' will herein be synonymous with 'surface dose', measured on a water phantom, and measurement points beyond a surface depth of 0.07 mm will be referred to as 'near-surface dose'. Based on our review of available literature, this would be the first published work of MOSFET's in a 1.5 T transverse MR-linac and the first published work of experimental skin dose, at a depth of 0.07 mm, in a 1.5 T transverse MR-linac. Experimental measurements with Gafchromic EBT-3 film (Ashland ISP Advanced Materials, NJ, USA) and simulations were also performed to compare to the MO*Skin*™ measurements.

Methodology

Measurements

MOSkin™ calibration

MO*Skin*™ detectors were calibrated on the Elekta Unity using the 7 MV FFF photon beam with a source-isocentre-distance (SID) of 143.5 cm, which coincides with a position 14.0 cm above the surface of the treatment couch. A 1.0 cm-thick custom-milled solid water (Gammex Solid Water- Model # 457, Middleton, WI) holder was manufactured such that the MO*Skin*™ was flush at the surface and without air gaps when placed at depth. The detectors were each placed face-up at the machine isocentre, at a 5.0 cm depth within a $15.0 \times 30.0 \times 30.0$ cm^3 solid water phantom, at a source-surface-distance (SSD) of 138.5 cm. For face-up MO*Skin*™ orientation, the WED to the SV is 0.07 mm whereas with a face-down orientation, the WED to the SV is approximately 0.9 mm [35].

The experimental set-up was verified using the megavoltage imager (MVI) panel that is integrated into the Elekta Unity system, and a machined aluminium ruler. This ruler consists of thirteen machined 3.0 mm circular holes along the central axis at 2.0 cm intervals. The ruler was placed on top of the phantom

blocks aligned with the y-axis. A schematic of the MO*Skin*™ calibration set-up with the coordinate system is shown in Fig. 1. Care was taken to reduce air gaps between the phantom slabs to minimise ERE. Using a 10 × 10 cm^2 field, gantry 90.0º (G90), 100 MU was delivered three times for each MO*Skin*™. G90 was used to avoid issues related to the variation of the helium level inside the cryostat. The average MO*Skin*™ read-out was calculated and used to determine a unique calibration factor for each detector to relate the threshold voltage shift to the dose deposited within the SV [35]. This Elekta Unity system is calibrated to give 1.0 Gy/100 MU to the isocentre at a depth of 5.0 cm in water, 138.5 cm SSD, for a 10 × 10 cm^2, G90, field.

Film calibration

EBT-3 film calibration was performed using 2.0 × 4.0 cm^2 film strips within a 30.0 × 30.0 × 19.0 cm^3 solid water phantom. Films were positioned at 5.0 cm depth within the phantom and irradiated with a G0 10 × 10 cm^2 field for 0, 100, 200, 400, and 800 MU. Films were scanned and digitised using an Epson Expression 12000XL flatbed scanner (Seiko. Epson Corporation, Nagano, Japan) in transmission mode, without colour correction and with a scan resolution of 75 DPI (0.34 mm pixel size), using 48-bit RGB mode. Multichannel analysis was used within the FilmQA™ Pro software (Ashland ISP Advanced Materials, NJ, USA) and lateral scanner variations were corrected using MATLAB (MathWorks Inc., MA) [36]. A central 1.0 × 1.0 cm^2 region of interest (ROI) on each film was used to correlate mean pixel values with the delivered dose.

MOSkin™ PDD

In-field percentage depth dose (PDD) curves were measured in a 20.0 × 30.0 × 30.0 cm^3 solid water phantom, containing the MOSkin™ and holder, with the phantom centre coincident with the isocentre. A face-up MOSkin™ orientation, relative to the primary beam direction, was used for all measurements. Due to the thin SV of the MOSkin™ device, volume averaging can be considered negligible and at the surface, the EPOM is equivalent to a WED of 0.07 mm. For consistency, all MOSkin™ measurement depths were expressed in terms of WED. Phantom dimensions were chosen to match the set-up from a previous investigation [17]. Again, the MVI and aluminium ruler were used for the phantom set-up. RTQA2 film (Ashland ISP Advanced Materials, NJ, USA) was used to verify the final alignment before measurements (Fig. 2a). For this study, entry and exit surfaces were flat and perpendicular to the beam direction to avoid significant dose variations that occur at oblique surfaces due to the ERE [11].

Depth dose measurements were acquired for 1 × 1 cm^2, 3 × 3 cm^2, 5 × 5 cm^2, 10 × 10 cm^2, and 22 × 22 cm^2 fields at G90 and 133.5 cm SSD. Readings in the build-up region were acquired at 0.07 mm, 0.12 mm, 0.17 mm, and 0.27 mm WEDs, with varying amounts of Polyimide (Kapton) tape (0.05 mm water equivalent thickness) over the detector surface for each measurement. Note that for photons energies > 1 MeV, the mass attenuation coefficient of Kapton and water closely match [37], [38]. In addition to the above, the MO*Skin*™ was also placed at physical depths 1.0 mm, 3.0 mm, 5.0 mm, 10.0 mm, and 13.0 mm that correspond to WEDs, relative to the primary beam direction, of 1.07 mm, 3.07 mm, 5.07 mm,

10.07 mm, and 13.07 mm, respectively. For exit beam measurements, the MOSkin™ was placed at physical depths 186.6 mm, 189.6 mm, 194.6 mm, 196.6 mm, 198.6 mm, and 199.6 mm, corresponding to WEDs of 186.67 mm, 189.67 mm, 194.67 mm, 196.67 mm, 198.67 mm, and 199.67 mm, respectively. For each depth, three measurements were acquired to obtain an average dose and standard deviation value. All dose measurements were normalised to that at the depth of maximum dose (d_{max}), approximately 13.0 mm for the Elekta Unity system [16].

Film PDD

PDD measurements with EBT-3 film required the use of an extended solid water phantom where film, 20.32 cm in length, was taped along the 20.0 cm phantom surface edge and sandwiched between an opposing solid water stack (Fig. 2b). This orientation had the long axis of the film parallel to the beam direction, G90, to record depth dose values with the fewest number of measurements. Both sides of the film were sprayed with water to minimise air gaps and reduce dose perturbations arising from ERE. The same fields as above were delivered with 500 MU. To avoid effects from film overhang at either surface, two films were individually irradiated for each field such that for one the film edge was flush with the phantom entry and similarly at the exit for the second film. Cutting the 20.32 cm film to a length of 20.0 cm was not an option as this delaminates the film and would render the dose near the cut edge inaccurate. After irradiation, films were scanned and analysed using the same method as above for calibration. Profiles along the central axis, averaged across 10 pixels, for each field size were acquired and normalised to the reading at d_{max}. Due to scan resolution, film entry and exit measurement points begin at a depth of 0.34 mm within the solid water phantom.

Simulations

Geant4

Simulations of the experimental geometry were performed using Geant4 and the Monaco treatment planning system (TPS) for comparison with measured data. The EPOM of Geant4 and Monaco TPS data corresponds to the centre of each scoring voxel. When comparing the simulation to experimental results, the WED to the centre of the respective voxel was used. Using Geant4 version 11.0.2, a $20.0 \times 30.0 \times 30.0$ cm^3 water equivalent block phantom ($\rho = 1.00$ g/cm^3) was created. With an SSD of 133.5 cm, beams were fired from phase space files (provided by Elekta) with a total of $1.12 \cdot 10^{10}$ primary histories per field size and a dose uncertainty of approximately ± 04 %. As specified in supporting documentation provided by Elekta, each phase space plane was located 129.5 cm from the source. The maximum step length was set to 0.01 mm. The dose within the phantom was scored using a $0.1 \times 1.0 \times 1.0$ mm^3 dose grid, where the dose along the direction of the beam (x-axis) was sampled at 0.1 mm increments. When determining depth dose profiles, adjacent voxels surrounding the central axis of the beam were averaged. For the smallest field size, 1×1 cm^2, two dose voxels in the y and z axes were averaged. This was scaled for

each field size such that for the 22 × 22 cm^2, 44 dose voxels in the y and z axes were averaged. For each beam, the depth dose curve was normalised to the reading at d$_{max}$.

Monaco TPS

For Monaco computations, a CT image of air was acquired with a 1.0 mm slice thickness and imported into the Monaco TPS (v5.4). A 20.0 × 30.0 × 30.0 cm^3 solid volume was contoured, centred to the isocentre, and set as the external structure. A forced relative electron density (RED) of 1.000 was applied to the contoured volume and couch structures were added. 1 × 1 cm^2, 3 × 3 cm^2, 5 × 5 cm^2, 10 × 10 cm^2, and 22 × 22 cm^2 500 MU, G90, beams were added. Calculations were performed using a 0.1 cm dose grid and a statistical uncertainty of 0.2% per control point. A transverse dose plane, centred at the isocentre, was exported for each field size. Dose planes were imported into Verisoft v7.2(PTW-Freiburg, Germany) where profiles were extracted. For each beam, the depth dose curve was normalised to the reading at d$_{max}$.

Results

Experimental surface and near-surface dose measurements with MO Skin ™ and film

Calibration factors determined for the two MO*Skin*™ detectors used in this work were (2.22 ± 0.03) mV/cGy and (2.22 ± 0.01) mV/cGy. MO*Skin*™ surface doses, 0.07 mm WED, at the beam entry were (9.9 ± 0.2) %, (10.1 ± 0.3) %, (11.3 ± 0.6) %, (12.9 ± 1.0) %, and (13.4 ± 1.0) % for 1 × 1 cm^2, 3 × 3 cm^2, 5 × 5 cm^2, 10 × 10 cm^2, and 22 × 22 cm^2 field sizes, respectively (Table 1). Measured near-surface film doses, at a depth of 0.34 mm along the PDD, were 33.8%, 34.4%, 31.3%, 36.5%, and 35.6% for all fields with an absolute difference of 20.1 – 24.3% to MO*Skin*™ surface doses. At a 0.27 mm WED, near-surface doses measured with the MO*Skin*™ were (20.8 ± 0.7) %, (18.7 ± 1.0) %, (19.3 ± 1.2) %, (21.1 ± 0.8) %, and (21.3 ± 0.9) % for the same fields and an absolute difference of 12.0-15.8% to film data.

Table 1: Comparison of surface and near-surface doses of the MOSkin™ detector with Geant4 and Monaco TPS calculations at the beam entry and beam exit of the phantom. Quoted doses are relative to d$_{max}$.

Field size (cm^2)	Entry (% d$_{max}$)			Exit (% d$_{max}$)		
	MO*Skin*™ WED = 0.07 mm	Geant4 WED = 0.05 mm	Monaco TPS WED = 0.50 mm	MO*Skin*™ WED = 199.67 mm	Geant4 WED = 199.95 mm	Monaco TPS WED = 199.50 mm
1 × 1	9.9 ± 0.2	9.3	26.3	37.2 ± 4.9	39.1	37.5
3 × 3	10.1 ± 0.3	10.5	24.0	50.0 ± 2.9	52.6	52.0
5 × 5	11.3 ± 0.6	11.1	24.2	54.9 ± 2.0	58.2	57.4
10 × 10	12.9 ± 1.0	12.0	24.9	63.9 ± 1.6	63.4	62.1
22 × 22	13.4 ± 1.0	13.1	26.1	62.4 ± 3.0	67.4	65.5

Similarly, MO*Skin*™ dose values when placed at the beam exit with a 199.67 mm WED, were (37.2 ± 4.9) %, (50.0 ± 2.9) %, (54.9 ± 2.0) %, (63.9 ± 1.6) % and (62.4 ± 3.0) %. At a depth of 199.66 mm, exit beam surface doses measured with film were 39.8 %, 55.3 %, 60.2 %, 61.1 %, and 68.1 % with a maximum absolute difference of 5.7 % to MO*Skin*™ values.

Fig.3 shows the full 20.0 cm phantom length PDD and subplots of the beam entry and exit PDDs for the 22 × 22 cm^2 field. Entry and exit PDD data for field sizes 1 × 1 cm^2, 3 × 3 cm^2, 5 × 5 cm^2, and 10 × 10 cm^2 is presented in Fig.4. Fractional uncertainties at each MOSkin™ measurement depth and the relative d$_{max}$ measurement, add in quadrature and are included as error bars and quoted uncertainties in Fig.3, Fig.4, Table 1, Table 2, and Table 3. Film dosimetry used in this investigation followed a protocol that yielded a dose uncertainty below 3.0 % [39].

MO Skin ™ comparison with Geant4 and Monaco TPS calculations

Monaco TPS and Geant4 depth dose curves are shown alongside experimental data in Fig. 3 and Fig. 4. A summary of the Monaco TPS, Geant4, and MO*Skin*™ normalised dose values at the beam entry and exit for each field size is shown in Table 1. Geant4 beam entry dose values, 0.05 mm WED, recorded 9.3%, 10.5%, 11.1%, 12.0%, and 13.1% for 1 × 1 cm^2, 3 × 3 cm^2, 5 × 5 cm^2, 10 × 10 cm^2, and 22 × 22 cm^2 field sizes, respectively with a maximum absolute difference and relative change of 1.0% and 7.4%, respectively across all fields compared to MO*Skin*™ results. Similarly, Monaco TPS reported near-surface dose values, 0.50 mm WED, were 26.3%, 24.0%, 24.2%, 24.9%, and 26.1%. Maximum absolute difference and relative change were 16.4% and 166.4%, respectively, compared to MO*Skin*™ results.

At the beam exit, the maximum absolute difference and relative change of MO*Skin*™ dose relative to Geant4 was 5.0% and 8.0%, respectively, and to Monaco TPS dose values, 3.1% and 5.0%, respectively, across all field sizes. For fields larger than 1 × 1 cm^2, Geant4 PDDs showed a field size-dependent dose increase at the exit due to the ERE. Between 187.0 mm and 200.0 mm, the increases were 11.2%, 14.2%, 16.4%, and 18.0% for the 3 × 3 cm^2, 5 × 5 cm^2, 10 × 10 cm^2, and 22 × 22 cm^2 field sizes, respectively. Similarly, increases of 11.7%, 14.7%, 16.0%, and 16.7% were found using Monaco TPS calculations.

Discussion

In this study when the MO*Skin*™ was placed at the exit surface orientated face-up relative to the primary beam direction, the silicon substrate included in the detector packaging, was exposed to air. Hence, there was the possibility that additional photon interactions within the thin silicon substrate, relative to water, could be produced and escape into the air, resulting in a larger measured exit dose, related to the ERE. The mass attenuation coefficient ratio of silicon to water is approximately equivalent above 0.2 MeV, hence the probability of photon interactions in the materials is approximately equal at these energies. Below this energy, the probability of photon interactions in silicon drastically increases and it cannot be considered water equivalent [37], [40]. The Elekta Unity system has an average photon beam energy of 2.11 MeV and a peak beam energy of 0.96 MeV [41], [42]. Of the total number of photon histories, few photons with energy below 0.2 MeV exist, hence no additional secondary electrons are expected, with the introduction of the silicon substrate, to contribute to the exit surface dose.

A comparison of MO*Skin*™ exit dose to Geant4 and Monaco TPS (Table 1), shows a maximum absolute difference and relative change of 5.0% and 8.0%, respectively, across all field sizes. This supports the above conclusion that the silicon substrate is not responsible for generating additional ERE dose, however, can itself attenuate low energy returning electrons and reduce the deposited energy within the SV. This effect was seen in all field sizes, except for the 10 × 10 cm^2, where MO*Skin*™ measurements were less than Geant4 and Monaco TPS dose values (Table 1). For a more accurate measurement of ERE skin dose, it is recommended to use a face-up MO*Skin*™ orientation, relative to the exit surface (i.e. the opposite orientation than was used in this investigation). With a MO*Skin*™ orientated face-up at the exit surface, returning electrons cross a 0.07 mm WED to the SV, as opposed to a 0.9 mm WED through the silicon substrate in the opposite MO*Skin*™ orientation.

MO*Skin*™ surface and near-surface doses were compared to OSLD measurements, performed by Kim *et al* [17], for the same irradiation conditions. Comparisons can be found in Table 2 and Table 3. Kim *et al* [17] also presented extrapolated surface doses to 0.0 mm and 0.07 mm depths; however, it is most appropriate to only consider data experimentally acquired at the shallowest depth of 0.16 mm when comparing to MO*Skin*™ surface (0.07 mm) measurements, due to uncertainties when extrapolating from two data points. MO*Skin*™ measured beam entry surface doses, 0.07 mm WED, were not within experimental uncertainty to published OSLD data, with a maximum absolute difference and relative change of 4.6% and 38.9%, respectively, for the three comparable field sizes. Better agreement to OSLD

data, with a maximum absolute difference and relative change of 1.1% and 6.5%, respectively, were found when comparing MO*Skin*™ near-surface measurements at a WED of 0.17 mm (Table 2).

Table 2: Entry MOSkin™ dose, normalised to 13.0 mm, compared with published OSLD data*, normalised relative to 15.0 mm [17]. MOSkin™ measurements acquired at WED of 0.07 mm and 0.17 mm are compared to existing near-surface OSLD measurements

	Entry (% d_{max})						
Field size (cm^2)	MO*Skin*™ WED = ^{1}0.07 mm	MO*Skin*™ WED = ^{2}0.17 mm	OSLD* WED = ^{3}0.16 mm	Absolute difference ($\Delta^{\|1-3\|}$)	Relative change ($\Delta^{(3-1)/1} \times 10\,\%$)	Absolute difference ($\Delta^{\|2-3\|}$)	Relative change ($\Delta^{(3-2)/2} \times 10\,\%$)
5 × 5	11.3 ± 0.6	15.3 ± 1.1	15.7	4.4	38.9	0.4	2.6
10 × 10	12.9 ± 1.0	16.2 ± 0.8	16.7	3.8	29.5	0.5	3.1
22 × 22	13.4 ± 1.0	16.9 ± 0.7	18.0	4.6	34.3	1.1	6.5

Table 3: Exit MOSkin™ dose, normalised to 13.0 mm, compared with published OSLD data*, normalised relative to 15.0 mm [17]. MOSkin™ measurements acquired at a 199.67 mm WED are compared to existing OSLD measurements at a similar depth

	Exit (% d_{max})			
Field size (cm^2)	MO*Skin*™ WED = ^{4}199.67 mm	OSLD* WED = ^{5}200.16 mm	Absolute difference ($\Delta^{\|4-5\|}$)	Relative change ($\Delta^{(5-4)/4} \times 10\,\%$)
5 × 5	54.9 ± 2.0	56.0	1.1	2.0
10 × 10	63.9 ± 1.6	62.8	1.1	-1.7
22 × 22	62.4 ± 3.0	63.4	1.0	1.6

The absolute difference and relative change of MO*Skin*™ beam entry surface dose measurements to film values reported by Woodings *et al* [16] were 23.3 % and 206.9 %, respectively, for a 5 × 5 cm^2 field, and 22.9 % and 177.4 %, respectively, for a 10 × 10 cm^2 field. Film data from our investigation (Fig.4) was

comparable to measurements by Wooding *et al* [16], with a maximum absolute difference of 3.3 %. Relative to MO*Skin*™, Geant4, Monaco TPS, and OSLDs measurements, film tends to overestimate surface dose at the beam entry. From this investigation, MO*Skin*™ near-surface beam entry measurements were found to better match published OSLD measurements [17] than published film data [16]; however, large discrepancies between OSLD near-surface measurements to 0.07 mm WED MO*Skin*™ data, were apparent (Table 2). Geant4 simulations validate MO*Skin*™ entry dose measurements and further support the feasibility of using the MO*Skin*™ to accurately measure beam entry surface dose. At the beam exit, MO*Skin*™ measurements agreed with OSLDs, within experimental error, for field sizes 5 × 5 cm^2, 10 × 10 cm^2 and 22 × 22 cm^2 with a maximum absolute difference and relative change of 1.1 % and 2.0 %, respectively (Table 3). Improved agreement between the two detectors at the exit is linked to a shallower dose gradient compared to the beam entrance.

In the build-up region, particularly within the first millimetre (Fig.3 and Fig.4), Geant4 dose calculations better match MO*Skin*™ measurements than Monaco TPS results. Due to volume averaging across the larger 1.0 mm voxel size in the steep dose gradient, Monaco TPS calculations were found to overestimate the entry dose. The maximum absolute difference and relative change were 16.4 % and 166.4 %, respectively, for all field sizes, compared to MO*Skin*™ surface doses. Beyond 1.0 mm at the beam entry, Monaco TPS and Geant4 PDD curves converge and only at the exit do they begin to slightly diverge (Fig.3 and Fig.4) when additional ERE dose is present. For all field sizes investigated, Monaco TPS and Geant4 PDD curves agreed, within 2.0 % (absolute difference), for depths beyond 1.0 mm.

The maximum absolute difference in film dose at the beam exit was 5.7 % across all fields relative to MO*Skin*™ measurements. A higher scan resolution of 254 DPI was also considered for the film analysis however it introduced large and incoherent variability along the PDD curves. Ordinarily, parallel film irradiation can produce smooth and continuous depth dose curves. However, in this investigation with the film placed in the transverse plane between four abutting solid water blocks that had varying surface flatness, air gaps were unavoidable despite water being used on the film and solid water block surfaces. Irradiating films parallel to the beam, in the coronal plane, within solid water blocks of dimensions 20´30 ´n cm^3 would minimise this issue; however, these were not available during this investigation. Film data, while noisy compared to Geant4 and Monaco TPS PDD curves, demonstrate that film can be useful to experimentally generate a continuous depth dose profile, whereas the MO*Skin*™ is point dose specific. The film data demonstrates the sensitivity of air gaps on film dosimetry in the MR-linac despite following a protocol that yields an uncertainty below 3.0 % [39].

For the 1 × 1 cm² field, no significant exit dose, due to ERE, was found (Fig.4b). This can be explained considering that for small fields, CPE conditions are not established [27] and a shift in the maximum exit dose away from the central axis occurs [11]. While the beam entry dose for the Elekta Unity is relatively independent of the field size, the exit dose and the net increase of dose, in the final 13.0 mm of the phantom, at the beam exit were found to be dependent on the field size for field sizes larger than a 1 × 1 cm² (Table 1). Though this may cause excess skin dose at a tissue-to-air boundary, using matched-opposing fields or *intensity-modulated radiation therapy* (*IMRT*) can minimise such effects [43]. In

addition, a water equivalent bolus of 1.0 cm placed at the exit surface can be used to significantly reduce ERE dose; however, this method is not often used clinically [11].

Previously, the MO*Skin*™ has been successfully used for in-vivo dosimetry (IVD) [29], [44]; and can be used in a passive mode for MR-linac dosimetry as the Kapton pigtail, inclusive in the MO*Skin*™ design, does not produce image distortions during MR imaging. For real-time dosimetry, when the Kapton pigtail is plugged into the current readout cable design, MR image distortions are introduced rendering the MO*Skin*™ unsuitable for real-time IVD on an MR-linac. When MR images are not being acquired, the MO*Skin*™ would be an ideal detector for measurements and provide real-time dose readout. The Centre of Medical Radiation Physics (CMRP) at the University of Wollongong, Australia is working to modify the existing cable design to avoid MR image noise and hence enable MO*Skin*™ real-time IVD during MR imaging.

Conclusion

For a transverse MR-linac, the dose at the beam entry is relatively independent of the field size. MO*Skin*™ skin dose recorded at the entry surface varied between (9.9 ± 0.2) % and (13.4 ± 1.0) %, expressed as a percentage of d_{max}, for the smallest and largest field sizes investigated. MO*Skin*™ entry surface doses agreed within 1.0% (absolute difference) to Geant4 calculations, compared to a 16.4% (absolute difference) discrepancy with Monaco TPS calculations, due to uncertainties introduced by the comparatively large voxel size. Exit dose increases, due to returning electrons, were found to be field size dependent. The 1 × 1 cm^2 field showed a minimal dose increase at the exit phantom surface that can be linked to a loss of CPE and a shift of the maximum exit dose away from the central axis. The MO*Skin*™ was able to measure the increase of exit ERE dose, within the final 13.0 mm of the phantom, and was in good agreement with a maximum absolute difference and relative change of 5.0% and 8.0% respectively, amongst all field sizes investigated, to Geant4 and Monaco TPS results. This study demonstrates that the MO*Skin*™ can be used for experimental surface dosimetry within a high field strength, transverse MR-linac and can estimate skin dose within an acceptable uncertainty. The investigation also validates the robustness of the Monaco TPS which agreed, within 2.0% (absolute difference), to Geant4 results for all field sizes investigated beyond 1.0 mm at the beam entry.

Declarations

Compliance with Ethical Standards

Conflict of interest:

Authors A. Rosenfeld and D.Cutajar declare consulting with Electrogenics Laboratories Ltd which is commercialising the MO*Skin*™ detector. Authors including P. Stokes, P. Metcalfe, J. Baines, and M. Powers have no relevant financial or non-financial interests to disclose.

Ethical approval: This article does not contain any studies with human participants or animals performed by any of the authors.

Authors' contribution statements:

Authors Elizabeth Patterson, Dean Cutajar, John Baines, Peter Metcalfe, and Marcus Powers contributed to the study's conception and design. Experimental data collection was performed by Elizabeth Patterson, Dean Cutajar, John Baines, Peter Metcalfe, and Marcus Powers. Experimental analysis and Monaco treatment planning system (TPS) simulations were performed by Elizabeth Patterson and Marcus Powers. Geant4 simulations were performed and analysed by Peter Stokes. The first draft of the manuscript was written by Elizabeth Patterson and authors including Peter Stokes, Anatoly Rosenfeld, John Baines, Peter Metcalfe, and Marcus Powers contributed to previous versions of the manuscript. All authors read and approved the final manuscript.

References

1. B. W. Raaymakers, A. J. E. Raaijmakers, A. N. T. J. Kotte, D. Jette, and J. J. W. Lagendijk, "Integrating a MRI scanner with a 6 MV radiotherapy accelerator: dose deposition in a transverse magnetic field," *Phys. Med. Biol.*, vol. 49, no. 17, p. 4109, Aug. 2004, doi: 10.1088/0031-9155/49/17/019.

2. A. J. E. Raaijmakers, B. W. Raaymakers, and J. J. W. Lagendijk, "Integrating a MRI scanner with a 6 MV radiotherapy accelerator: dose increase at tissue–air interfaces in a lateral magnetic field due to returning electrons," *Phys. Med. Biol.*, vol. 50, no. 7, p. 1363, Mar. 2005, doi: 10.1088/0031-9155/50/7/002.

3. E. Y. Han *et al.*, "Measurement of Electron Return Effect and Skin Dose Reduction by a Bolus in an Anthropomorphic Physical Phantom under a Magnetic Resonance Guided Linear Accelerator (MR-LINAC) System," *Int. J. Med. Physics, Clin. Eng. Radiat. Oncol.*, vol. 7, no. 3, pp. 339–346, Jun. 2018, doi: 10.4236/IJMPCERO.2018.73028.

4. A. J. E. Raaijmakers, B. W. Raaymakers, and J. J. W. Lagendijk, "Magnetic-field-induced dose effects in MR-guided radiotherapy systems: Dependence on the magnetic field strength," *Phys. Med. Biol.*, vol. 53, no. 4, pp. 909–923, 2008, doi: 10.1088/0031-9155/53/4/006.

5. A. J. E. Raaijmakers, B. W. Raaymakers, and J. J. W. Lagendijk, "Experimental verification of magnetic field dose effects for the MRI-accelerator," *Phys. Med. Biol.*, vol. 52, no. 14, p. 4283, Jun. 2007, doi: 10.1088/0031-9155/52/14/017.

6. C. Y. Huang *et al.*, "Effects on skin dose from unwanted air gaps under bolus in an MR-guided linear accelerator (MR-linac) system," *Phys. Med. Biol.*, vol. 66, no. 6, p. 065021, Mar. 2021, doi: 10.1088/1361-6560/abe837.

7. D. J. O'Brien, J. Dolan, S. Pencea, N. Schupp, and G. O. Sawakuchi, "Relative dosimetry with an MR-linac: Response of ion chambers, diamond, and diode detectors for off-axis, depth dose, and output factor measurements: Response," *Med. Phys.*, vol. 45, no. 2, pp. 884–897, 2018, doi: 10.1002/mp.12699.

8. B. M. Oborn, P. E. Metcalfe, M. J. Butson, and A. B. Rosenfeld, "High resolution entry and exit Monte Carlo dose calculations from a linear accelerator 6 MV beam under the influence of transverse magnetic fields," *Med. Phys.*, vol. 36, no. 8, pp. 3549–3559, 2009, doi: 10.1118/1.3157203.

9. A. J. E. Raaijmakers, B. W. Raaymakers, S. Van Der Meer, and J. J. W. Lagendijk, "Integrating a MRI scanner with a 6 MV radiotherapy accelerator: Impact of the surface orientation on the entrance and exit dose due to the transverse magnetic field," *Phys. Med. Biol.*, vol. 52, no. 4, pp. 929–939, 2007, doi: 10.1088/0031-9155/52/4/005.

10. S. Wegener, S. Weick, and O. A. Sauer, "Influence of a transverse magnetic field on the response of different detectors in a high energy photon beam near the surface," *Z. Med. Phys.*, vol. 29, no. 1, pp. 22–30, Feb. 2019, doi: 10.1016/J.ZEMEDI.2018.07.001.

11. B. M. Oborn, P. E. Metcalfe, M. J. Butson, and A. B. Rosenfeld, "Monte Carlo characterization of skin doses in 6 MV transverse field MRI-linac systems: Effect of field size, surface orientation, magnetic field strength, and exit bolus," *Med. Phys.*, vol. 37, no. 10, pp. 5208–5217, 2010, doi: 10.1118/1.3488980.

12. B. Yang *et al.*, "Measurement of surface dose in a 1.5 T MR-Linac using plane-parallel ionization chamber," in *ESTRO: PO-1343*, 2020, doi: 10.3252/pso.eu.ESTRO2020.2020.

13. P. A. Jursinic and T. R. Mackie, "Characteristics of secondary electrons produced by 6, 10 and 24 MV x-ray beams," *Phys. Med. Biol.*, vol. 41, no. 8, p. 1499, Aug. 1996, doi: 10.1088/0031-9155/41/8/016.

14. S. J. Woodings *et al.*, "Performance of a PTW 60019 microDiamond detector in a 1.5 T MRI-linac," *Phys. Med. Biol.*, vol. 63, no. 5, p. 05NT04, Mar. 2018, doi: 10.1088/1361-6560/AAA1C6.

15. M. Nachbar *et al.*, "Partial breast irradiation with the 1.5 T MR-Linac: First patient treatment and analysis of electron return and stream effects," *Radiother. Oncol.*, vol. 145, pp. 30–35, 2020, doi: 10.1016/j.radonc.2019.11.025.

16. S. J. Woodings *et al.*, "Beam characterisation of the 1.5 T MRI-linac," *Phys. Med. Biol.*, vol. 63, no. 8, p. 085015, Apr. 2018, doi: 10.1088/1361-6560/aab566.

17. A. Kim, S. Lim-Reinders, S. B. Ahmad, A. Sahgal, and B. M. Keller, "Surface and near-surface dose measurements at beam entry and exit in a 1.5 T MR-Linac using optically stimulated luminescence dosimeters," *Phys. Med. Biol.*, vol. 65, no. 4, p. 045012, Feb. 2020, doi: 10.1088/1361-6560/AB64B6.

18. S. Lim-Reinders, B. M. Keller, A. Sahgal, B. Chugh, and A. Kim, "Measurement of surface dose in an MR-Linac with optically stimulated luminescence dosimeters for IMRT beam geometries," *Med. Phys.*, vol. 47, no. 7, pp. 3133–3142, Jul. 2020, doi: 10.1002/MP.14185.

19. Y. Zhang *et al.*, "Out-of-field dose assessment for a 1.5 T MR-Linac with optically stimulated luminescence dosimeters," *Med. Phys.*, vol. 48, no. 7, pp. 4027–4037, Jul. 2021, doi: 10.1002/mp.14839.

20. E. Y. Han, Z. Wen, H. J. Lee, A. dela C. Paulino, and C. Lee, "Measurement of Electron Return Effect and Skin Dose Reduction by a Bolus in an Anthropomorphic Physical Phantom under a Magnetic Resonance Guided Linear Accelerator (MR-LINAC) System," *Int. J. Med. Physics, Clin. Eng. Radiat. Oncol.*, vol. 07, no. 03, pp. 339–346, 2018, doi: 10.4236/ijmpcero.2018.73028.

21. P. Yadav, A. Hallil, D. Tewatia, D. A. P. Dunkerley, and B. Paliwal, "MOSFET dosimeter characterization in MR-guided radiation therapy (MRgRT) Linac," *J. Appl. Clin. Med. Phys.*, vol. 21, no. 1, pp. 127–135, Jan. 2020, doi: 10.1002/ACM2.12799.

22. B. A. Mcdonald, H. J. Lee, and G. S. Ibbott, "Low-density gel dosimeter for measurement of the electron return effect in an MR-linac*," *Phys. Med. Biol.*, vol. 64, no. 20, p. 205016, Oct. 2019, doi: 10.1088/1361-6560/AB4321.

23. K. Smit, B. Van Asselen, J. G. M. Kok, A. H. L. Aalbers, J. J. W. Lagendijk, and B. W. Raaymakers, "Towards reference dosimetry for the MR-linac: magnetic field correction of the ionization chamber reading," *Phys. Med. Biol.*, vol. 58, no. 17, p. 5945, Aug. 2013, doi: 10.1088/0031-9155/58/17/5945.

24. T. Tekin, I. Blum, B. Delfs, A. B. Schönfeld, B. Poppe, and H. K. Looe, "The magnetic field dependent displacement effect and its correction in reference and relative dosimetry," *Phys. Med. Biol.*, vol. 67, no. 4, Feb. 2022, doi: 10.1088/1361-6560/AC4A41.

25. PTW Freiburg, "Including Codes of Practice Detectors for Ionizing Radiation," Freiburg, Germany, Jul. 2022.

26. ICRP, "Annals of the ICRP Published on behalf of the International Commission on Radiological Protection Members of the Main Commission of the ICRP," 1990. doi: 10.1177/ANIB_21_1-3.

27. I. J. Das *et al.*, "Report of AAPM Task Group 155: Megavoltage photon beam dosimetry in small fields and non-equilibrium conditions," *Med. Phys.*, vol. 48, no. 10, pp. e886–e921, Oct. 2021, doi: 10.1002/MP.15030.

28. I. Billas, H. Bouchard, U. Oelfke, and S. Duane, "The effect of magnetic field strength on the response of Gafchromic EBT-3 film," *Phys. Med. Biol.*, vol. 64, no. 6, p. 06NT03, Mar. 2019, doi: 10.1088/1361-6560/AB0503.

29. M. Carrara *et al.*, "Clinical application of MOSkin dosimeters to rectal wall in vivo dosimetry in gynecological HDR brachytherapy," *Phys. Medica*, vol. 41, pp. 5–12, Sep. 2017, doi: 10.1016/J.EJMP.2017.05.003.

30. S. Exhibit, N. Thorpe, A. Rosenfeld, P. Metcalfe, D. Cutajar, and M. Cai, "Development of quality assurance dosimetry systems for MRI brachytherapy and MRI-Linac technology," pp. 1–21, 2014.

31. N. F. Roberts *et al.*, "Experimental characterization of magnetically focused electron contamination at the surface of a high-field inline MRI-linac," *Med. Phys.*, 2019, doi: 10.1002/mp.13847.

32. E. Patterson *et al.*, "Characterizing magnetically focused contamination electrons by off-axis irradiation on an inline MRI-Linac," *J. Appl. Clin. Med. Phys.*, vol. 23, no. 6, Jun. 2022, doi:

10.1002/ACM2.13591.

33. M. Tai, E. Patterson, P. E. Metcalfe, A. Rosenfeld, and B. M. Oborn, "Skin Dose Modeling and Measurement in a High Field In-Line MRI-Linac System," *Front. Phys.*, vol. 0, p. 512, Jun. 2022, doi: 10.3389/FPHY.2022.902744.

34. A. Rozenfeld, "Radiation sensor and dosimeter US Patent, US8742357B2," Jun. 02, 2008.

35. W. L. Jong *et al.*, "Characterization of MOSkin detector for in vivo skin dose measurement during megavoltage radiotherapy," *J. Appl. Clin. Med. Phys.*, vol. 15, no. 5, pp. 120–132, 2014, doi: 10.1120/JACMP.V15I5.4869.

36. A. Micke, D. F. Lewis, and X. Yu, "Multichannel film dosimetry with nonuniformity correction," *Med. Phys.*, vol. 38, no. 5, pp. 2523–2534, May 2011, doi: 10.1118/1.3576105.

37. "NIST: X-Ray Mass Attenuation Coefficients - Water, Liquid." https://physics.nist.gov/PhysRefData/XrayMassCoef/ComTab/water.html (accessed Jul. 20, 2022).

38. H. C. Manjunatha, "A study of gamma attenuation parameters in poly methyl methacrylate and Kapton," *Radiat. Phys. Chem.*, vol. 137, pp. 254–259, Aug. 2017, doi: 10.1016/J.RADPHYSCHEM.2016.01.024.

39. M. Van Der Walt, L. Marsh, J. Baines, S. Gibson, A. Shoobridge, and · Glenn De Vine, "Performance evaluation of an LED flatbed scanner for triple channel film dosimetry with EBT3 and EBT-XD film," *Phys. Eng. Sci. Med. 2022 453*, vol. 45, no. 3, pp. 901–914, Aug. 2022, doi: 10.1007/S13246-022-01161-Z.

40. "NIST: X-Ray Mass Attenuation Coefficients - Silicon." https://physics.nist.gov/PhysRefData/XrayMassCoef/ElemTab/z14.html (accessed Sep. 09, 2022).

41. M. Yano, F. Araki, and T. Ohno, "Monte Carlo study of small-field dosimetry for an ELEKTA Unity MR-Linac system," *Radiat. Phys. Chem.*, vol. 194, p. 110036, May 2022, doi: 10.1016/J.RADPHYSCHEM.2022.110036.

42. K. Smit, "Dosimetry for the MR-linac," pp. 1–139, Jul. 2015, Accessed: Sep. 08, 2022. [Online]. Available: https://dspace.library.uu.nl/handle/1874/318363.

43. A. J. E. Raaijmakers, B. Hårdemark, B. W. Raaymakers, C. P. J. Raaijmakers, and J. J. W. Lagendijk, "Dose optimization for the MRI-accelerator: IMRT in the presence of a magnetic field," *Phys. Med. Biol.*, vol. 52, no. 23, p. 7045, Nov. 2007, doi: 10.1088/0031-9155/52/23/018.

44. W. L. Jong *et al.*, "In vivo skin dose measurement using MOSkin detectors in tangential breast radiotherapy," *Phys. Med.*, vol. 32, no. 11, pp. 1466–1474, Nov. 2016, doi: 10.1016/J.EJMP.2016.10.022.
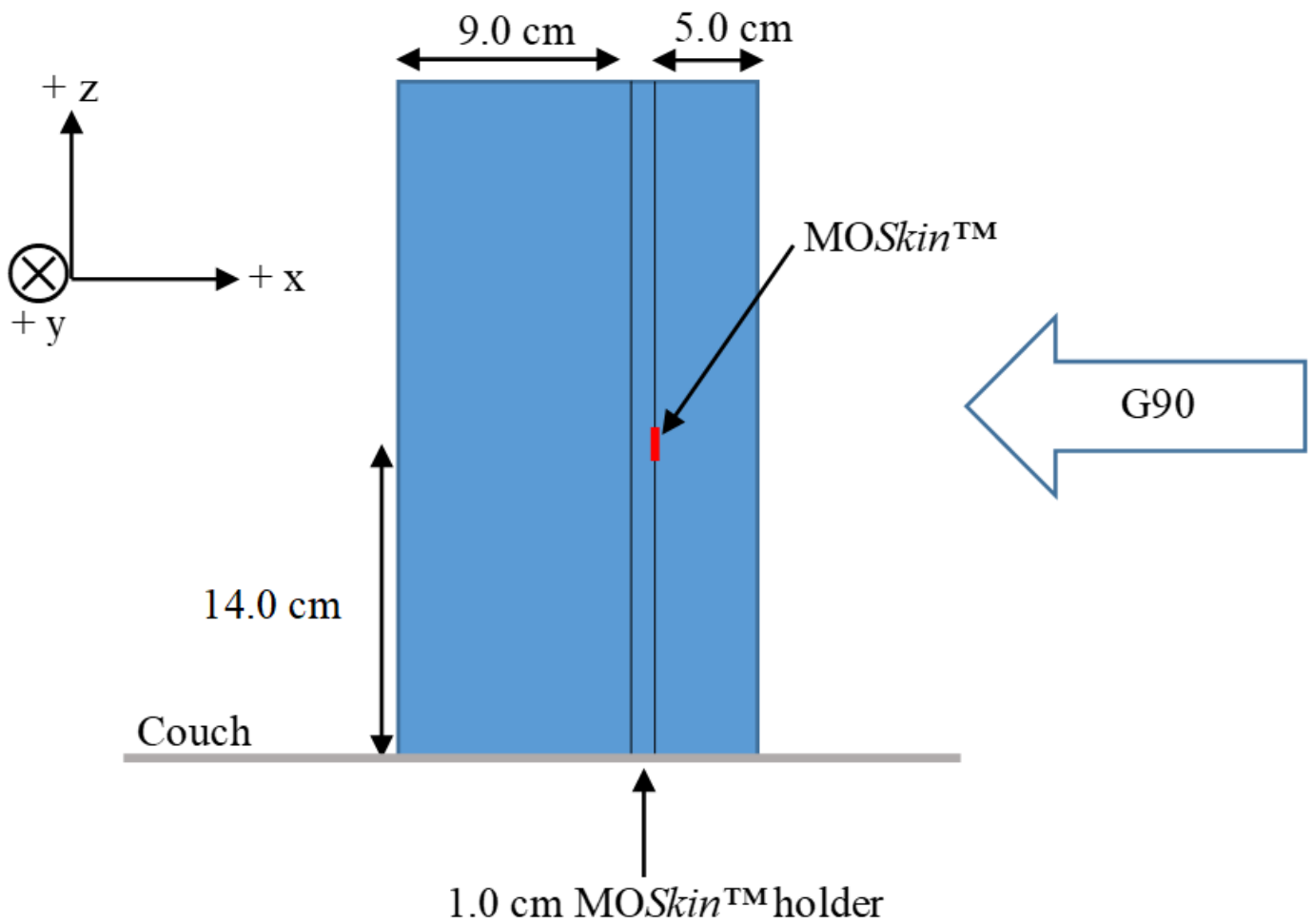
Figures

Figure 1

Schematic of the set-up used to calibrate the MOSkin™ detectors. The MOSkin™ was placed at the machine isocentre 14.0 cm above the couch surface, and at a depth of 5.0 cm. The IEC-61217 coordinate system is shown in the top left of the image. The arrow with 'G90' inside, indicates the beam direction and B_0 is directed out of the page, parallel to the y-axis
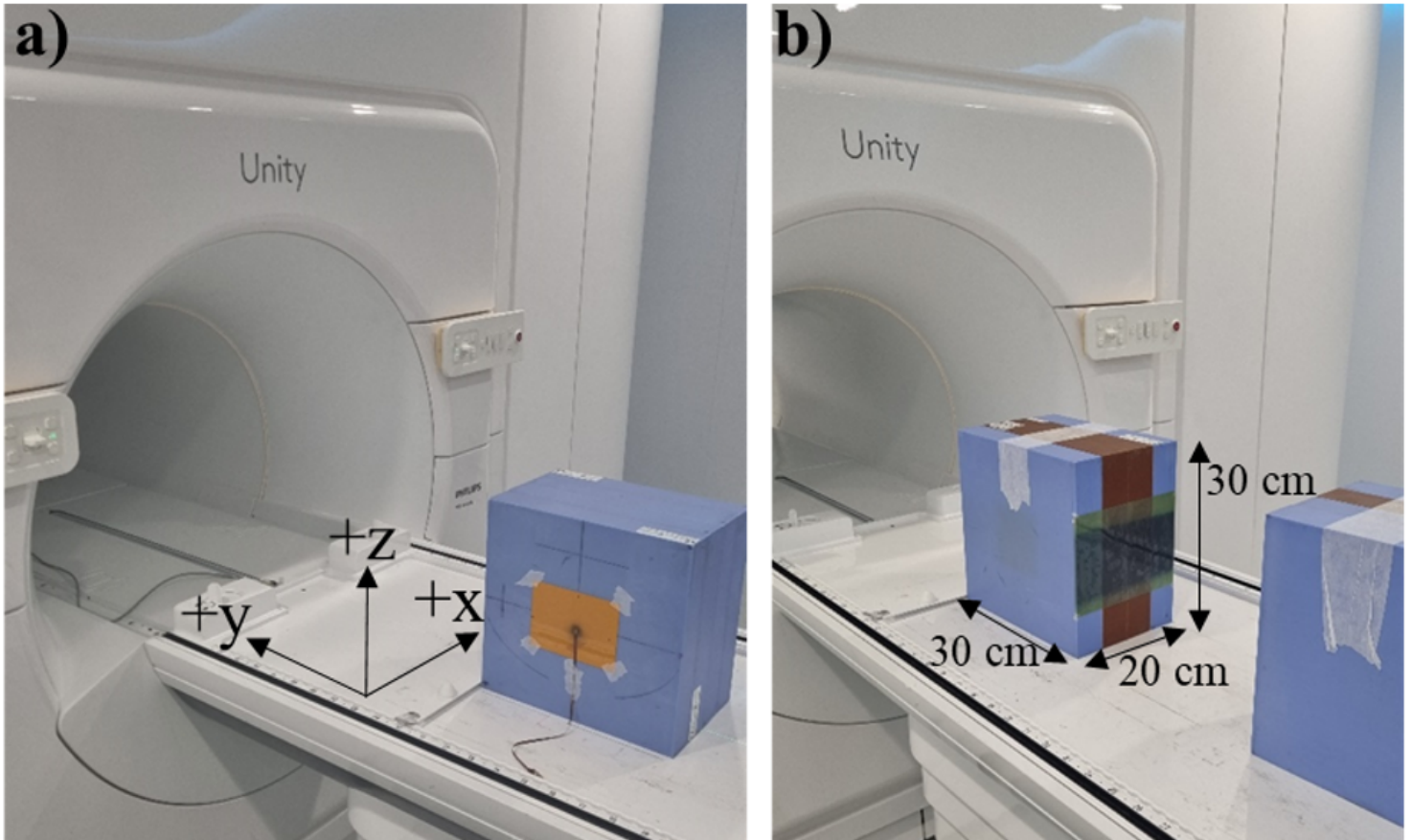
Figure 2

a) MOSkin™ positioning verified using RTQA2 film at the exit surface of the 20.0 × 30.0 × 30.0 cm^3 solid water phantom for a 1 × 1 cm^2 field size. b) EBT-3 film placement for depth dose measurements. Water was applied to both sides of the film to minimise air bubbles between the solid water blocks
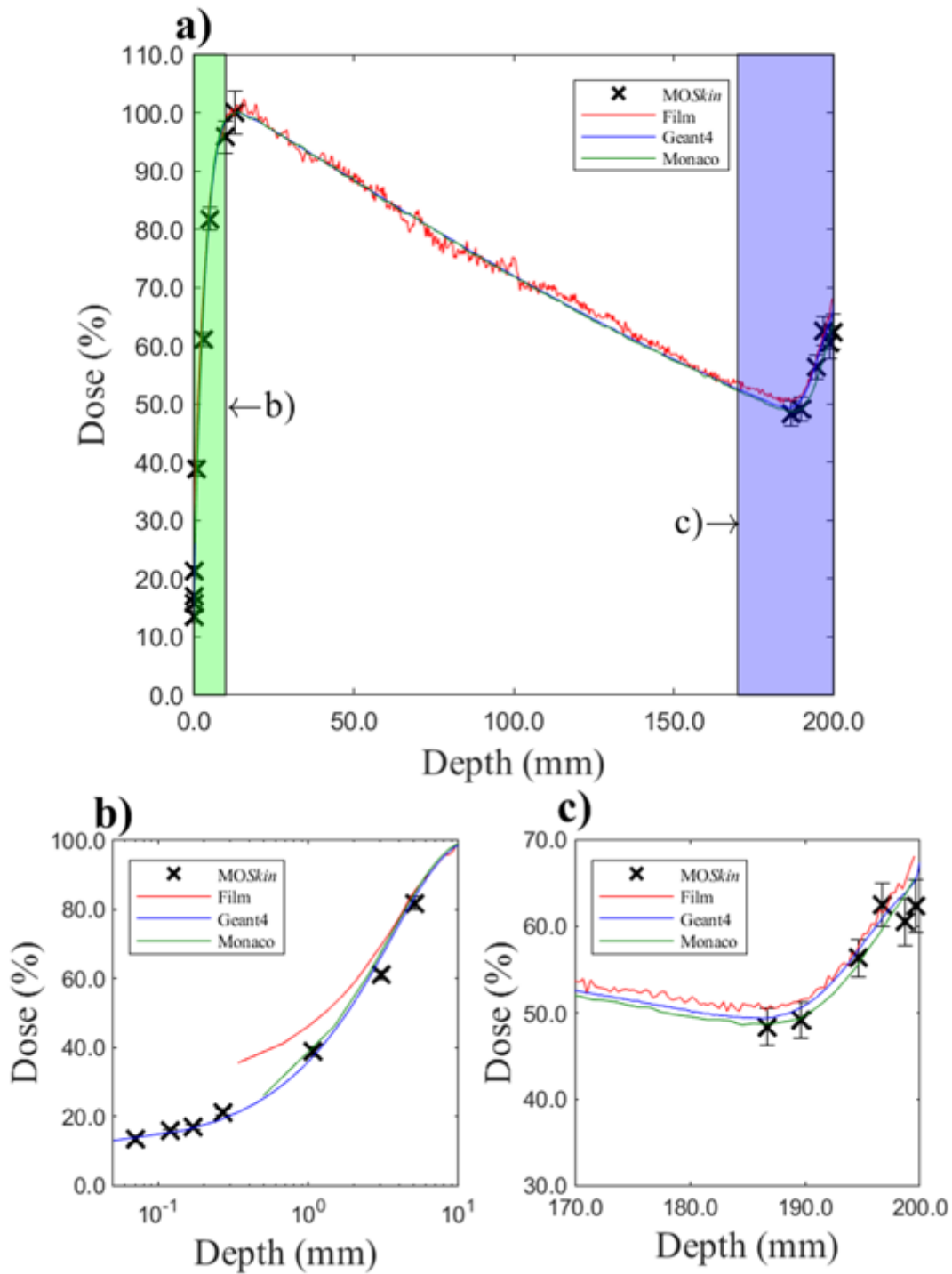
Figure 3

a) Full length experimental and simulation phantom PDDs, normalised to d_{max}, for the 22 × 22 cm² field size. The green and purple shaded regions in a) are magnified in b) and c), for clarity and represent the first 10.0 mm and last 30.0 mm depth of the PDD. A log scale has been used for the x-axis in b) to resolve the data points
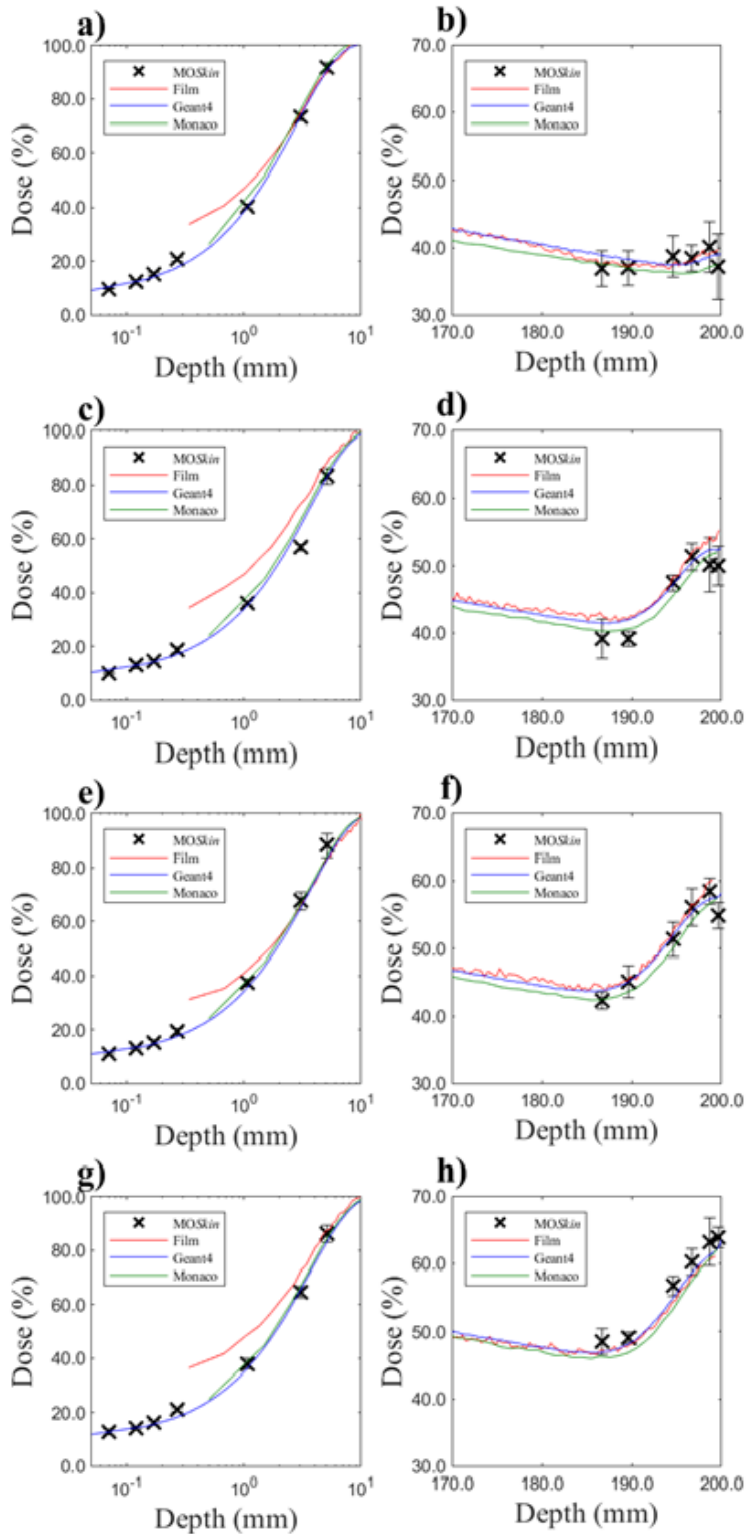
Figure 4

Magnified PDDs, normalised to d_{max}, with Monaco TPS and Geant4 calculations overlaid with experimental MOSkin™ and film measurements. Subplots a), c), e), and g) show entry PDDs for the first 10.0 mm (x-axis log scale) for field sizes 1 × 1, 3 × 3, 5 × 5, and 10 × 10 cm². Subplots b), d), f), and h) show exit PDDs in the last 30.0 mm of the phantom for the same fields